µFLU08-183

COARSE GRID MODELLING OF CAPILLARY DRIVEN TWO-PHASE FLOW IN DIRECT METHANOL FUEL CELLS

Paust, Nils
nils.paust@imtek.de

Koltay, Peter; Zengerle, Roland; Ziegler, Christoph

KEY WORDS

Passive DMFC, computational fluid dynamics, bubble driven micropump, contact angle hysteresis

ABSTRACT

A simulation study of two phase flow at the anode of a passive Direct Methanol Fuel Cell (DMFC) operating without any pumps and valves is presented. Passive operation is achieved by using the surface energy of deformed CO_2 bubbles to propel fuel circulation. Modeling the passive supply mechanism is supposed to shed light on the influence of bubble generation, contact angle dynamics and bubble venting on the capillary force induced transport of the water methanol solution. Simulating the anode process in detail is computationally very demanding. Therefore, the present work follows a coarse grid modelling approach: The capillary transport is resolved by solving Navier-Stokes equations on a finite volume computational grid. The Volume of Fluid (VoF) method with standard models accounting for surface tension effects is applied to track the free interfaces of CO_2 bubbles. Phenomena on a smaller scale, such as bubble nucleation, bubble venting and triple line phenomena are accounted for by additional sub models. The presented model allows for stable simulation of a complete bubble driven pump cycle in a single channel of the DMFC. Results are presented that show the influence of bubble merge, gas venting and contact angle hysteresis on the liquid flow rates induced by the moving bubble.

1 INTRODUCTION

Recently, so called passive concepts for fueling direct methanol fuel cells (DMFCs) have been proposed [1-4]. The scope of these concepts is to supply the fuel cells without the use of external pumps and valves. The DMFC system becomes smaller and more compact and the overall energy density is increased. These passive DMFC systems are especially attractive when a self-sufficient long-term power supply is desired that is easily rechargeable. However, among others, the reaction product carbon dioxide, produced by the electrochemical conversion at the anode of a DMFC, poses a significant challenge. The carbon dioxide nucleates to gas bubbles that may block channels, hinder fuel supply and can cause the DMFC to malfunction. To account for this challenge, we have proposed a passive supply mechanism that combines gas bubble removal and fuel supply [5]. In the present work, this supply mechanism is analyzed by two-phase Computational Fluid Dynamics (CFD) simulations.

2 WORKING PRINCIPLE

The passive supply mechanism is propelled by the surface energy of CO_2 bubbles, deformed in a tapered channel. As depicted in Fig.1, such a bubble forms interfaces with different curvatures at both bubble ends. According to the law of Young Laplace, the different curvatures κ_b and κ_f lead to a pressure difference across the bubble given by:

$$\Delta p_{bubble} = 2\sigma\left(\kappa_b - \kappa_f\right)$$

(1)

where σ is the surface tension of the liquid-gas interface. This pressure difference causes the bubble to move in the direction of increasing channel height. At the same time, induced by the moving bubbles, liquid is pumped through the channel. Depending on the size of the moving bubbles, a blocking and a non-blocking pumping mode can be realized. As schematically depicted in Fig.2, a moving bubble blocking the channel transports the major part of the displaced liquid out of the channel that means that liquid is effectively pumped. A minor part flows to the back of the bubble due to corner flow at the channel edges. In the non-blocking mode (Fig.2 (b)), a liquid bypass remains so that the major part of the displaced liquid flows directly around the bubble, hence no contribution to the pumping mechanism is made. The size of the bubbles that detach from the initial point of growth depends on geometry and wetting properties of the channel walls. By varying the contact angle or the opening angle of the tapered channel, the pumping modes can be changed.
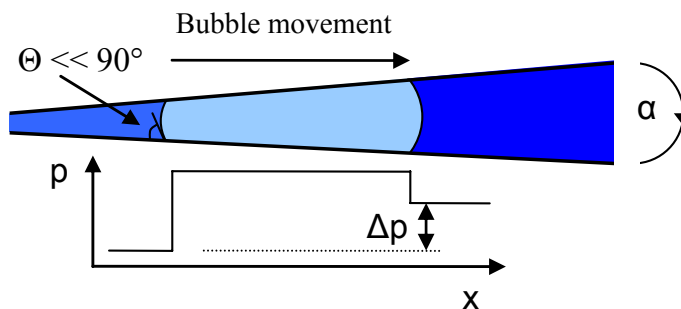
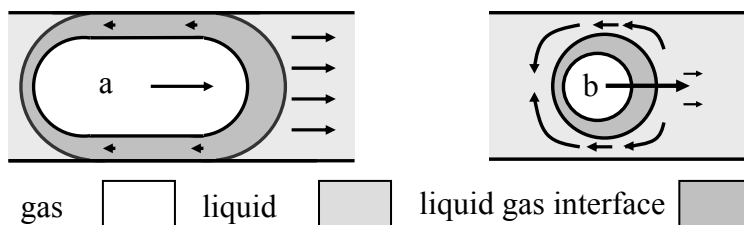**Figure 1:** Schematic of a deformed bubble inside a tapered channel.

Figure 2: Schematic top view of moving bubbles in a tapered channel. a) Blocking mode and b) non-blocking mode.

Fig.3 shows a schematic of a DMFC with the passive supply mechanism incorporated. In order to investigate the influence and interaction of bubble generation, capillary driven movement, and the gas venting through the porous membrane, a model of the passive supply mechanism has been developed. In the following, this model is presented and discussed.
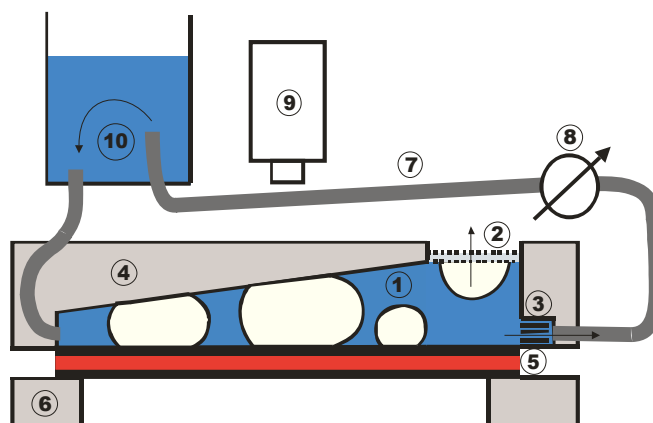
Figure 3: Schematic of a fully passive DMFC: 1) Tapered channel 2) Hydrophobic membrane 3) Bubble fence 4) Transparent anode flow field 5) GDL and MEA 6) Cathode flow field 7) Tubing 8) Flow sensor 9) Camera 10) Reservoir.

3   NUMERICAL MODEL

The computational domain is depicted in Fig.4. Unsteady, isothermal laminar flow conditions are assumed to prevail for both liquid and gas flow. The velocity field is governed by the Navier-Stokes equation:

$$\frac{\partial \rho \vec{v}}{\partial t} + \nabla \bullet (\rho \vec{v} \vec{v}) = -\nabla p + \eta \Delta \vec{v} + S_{\vec{v}} \qquad (2)$$

The continuity equation is used to couple the pressure and velocity fields as described in [6].

$$\frac{\partial \rho}{\partial t} + \nabla \bullet (\rho \vec{v}) = S_m \qquad (3)$$

In Eq.(2) and (3) $\vec{v}$ is the velocity vector, ρ and η are the average fluid density and viscosity, p denotes the static pressure and $S_{\vec{v}}$ and S_m are momentum and mass source terms, respectively. For tracking the free interfaces of the bubbles, the Volume of Fluid (VoF) method [7] is applied. A single set of equations is solved for both fluids and the phases are tracked by an additional passive transport equation:

$$\frac{\partial F}{\partial t} + \nabla \bullet \vec{v} F = 0 \qquad (4)$$

where F describes the phase distribution with the following relation:

$$F_n = \begin{cases} 0 & \text{(gas)} \\ 1 & \text{(liquid)} \\ 0 < F < 1 & \text{(interface)} \end{cases} \qquad (3)$$

For Eq.(2), the average density and viscosity is calculated as described in [8]. Within the VoF method, the Piecewise Linear Interface Construction (PLIC) scheme is used to construct homogeneous interfaces from the F-distribution. The Continuum Surface Force (CSF) [9] model is applied that accounts for the pressure jump across a liquid gas interface. A drawback of VoF in combination with PLIC and CSF is that a small time step is required to achieve convergence. For stability reasons, the propagation of the interface in each computational cell is restricted by:

$$\Delta t_c = C \frac{d_c}{|\vec{v}|} \qquad (4)$$

where Δt_c is the time step, C the Courrant number and d_c the diameter of the computational cell. Eq.(4) is solved in any cell containing an interface and the minimum Δt_c is used as the time step Δt.
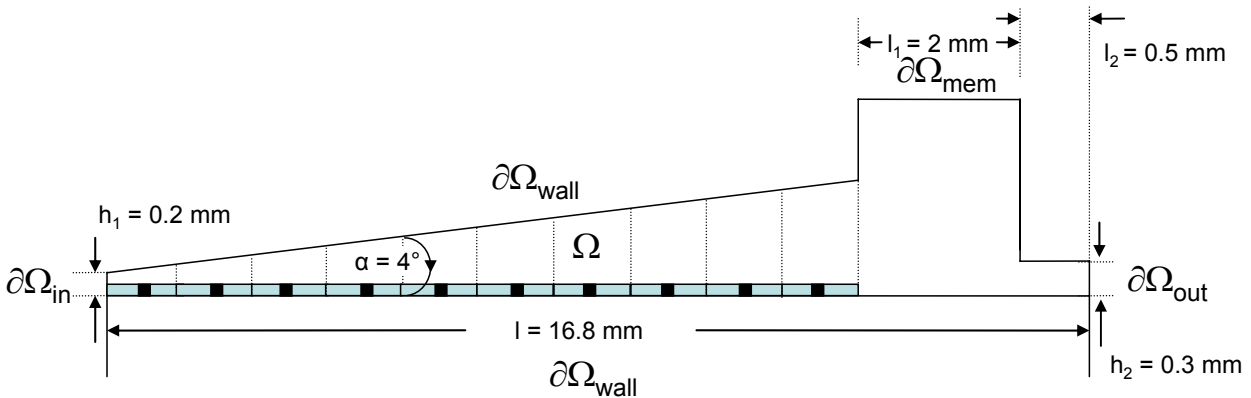

Figure 4: Computational domain. The depth of the computation domain is 0.6 mm covering the half of the actual channel with $\partial \Omega_{wall}$ on one side and a symmetry boundary condition on the other. For bubble generation, the domain Ω is subdivided into 10 control volumes as depicted. The black squares contain the computational cells in which the source terms are applied.

The no-slip boundary condition is imposed along the channel walls $\partial \Omega_{wall}$ and the contact angle is specified. For the channel in- and outlets, a pressure boundary condition is used. Since no external actuation is applied, at the in- and outlet the pressure is set to ambient pressure. Due to symmetry of a single channel, half of the channel is meshed and a symmetry boundary condition is applied. $\partial \Omega_{mem}$ contains a no-slip boundary condition for the liquid phase and a phase specific sink term for the gas phase.

A major challenge for modelling the passive supply mechanism is the computational cost of the performed simulations. The simulation of the capillary pumping mechanism is a multi-scale problem in space and in time. In order to analyze the performance of a complete pumping cycle, defined as the period of time that a gas bubble occurring next to the inlet requires to move through the channel and leave the system through the porous membrane, a time period of the order of magnitudes of a few seconds must be simulated. Depending on grid size and the local velocities in the domain, the time step size calculated with Eq.(4) is between 10^{-4}s and 10^{-6}s. Therefore, up to a million time steps must be computed for each cell. To keep the computational cost as small as possible, the capillary pump mechanism is resolved with as little cells as possible still leading to stable simulations. Performing a grid convergence study with the full model requires several weeks of computation, therefore, the minimum amount of cells has been determined by two separate grid convergence studies: A single phase flow study in the complete domain in which the pressure loss was analyzed for the highest flow rate occurring during the pump performance and a two phase study applying the VoF and CSF method analyzing the calculated capillary pressure across the interfaces of a single bubble. In Fig.5, the pressure difference from the inlet to the outlet of the domain depicted in Fig.4 is plotted against the number of cells used for the spatial resolution of the channel height. It can be seen that the pressure difference converges at a resolution of 14 cells across the channel height.

For the investigation of the grid dependency of the capillary pressure, the simulated pressure difference across the interfaces of a spherical bubble Δp_{sim} is compared to the pressure difference calculated by the Young Laplace Equation:

$$\Delta p = \frac{2\sigma}{r_{bub}} \tag{5}$$

where r_{bub} is the radius of the bubble. Simulations are performed for 2 ms with a time step of 10^{-6}s in a cubic domain with 20^3 cells. The relative error of the calculated pressure plotted against the cube root of cells filled by the bubble is depicted in Fig.6. It can be seen that for more than 8^3 cells the relative error is smaller than 0.005 and remains constant even if the resolution is increased further. The reason for the convergence is that the spatial resolution of 8^3 cells is sufficient when using the PLIC interface construction scheme for the calculation of the surface curvature of the bubbles. For less than 5^3 cells, divergence of the momentum equation is observed and the bubble falls into pieces.
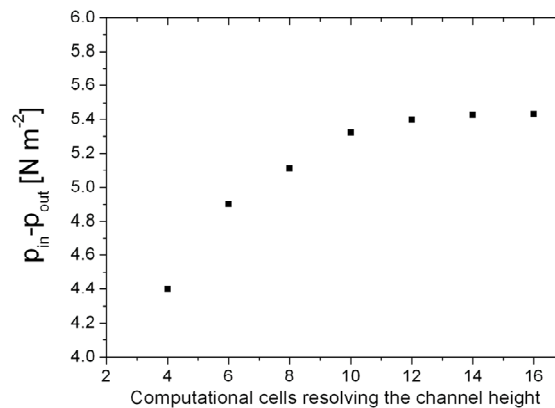

Figure 5: Pressure difference from channel inlet to channel outlet in the domain depicted in Fig.4 plotted against the number of computational cells across the channel height.

According to the grid convergence study, for the present two-phase simulations, the channel height is resolved by 14 computational cells. The smallest simulated bubbles fill 8^3 cells. Phenomena requiring a higher resolution are addressed by additional sub models. Triple line phenomena are accounted for by a model for the dynamic contact angle in particular accounting for contact angle hysteresis as explained in [10], gas venting is simulated by a sink term added to Eq.(2), and bubble generation is accounted for by source terms in Eq.(2). The bubble nucleation model is presented in the following. Details of the contact angle model and the gas venting model are discussed in [11].
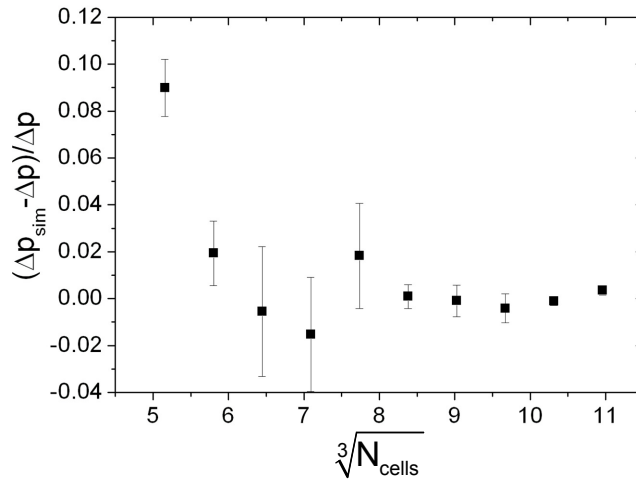
Figure 6: Relative error of the simulated pressure difference across the interfaces of single bubbles plotted against the cube root of the number of cells filled by the bubble.

3.1 Bubble generation

At a given specific current I of the operating fuel cell, the mass flow of the generated carbon dioxide per unit area of the MEA can be calculated as:

$$\dot{m}_{CO2} = \frac{I}{6\text{Fa}} M_{CO_2}. \tag{5}$$

Here, M_{CO2} is the molar mass of carbon dioxide, and Fa is the Faraday constant. For passive operation, it is assumed that the liquid is saturated with CO_2, therefore, all generated CO_2 is assumed to form bubbles. For the simulation, gas bubbles must be generated at the channel bottom with a rate fulfilling Eq.(5).

According to the grid study, the capillary pressure is accurately resolved for bubbles filling more than 8^3 cells. Smaller bubbles do not touch both channel walls, therefore their liquid gas interfaces do not contribute to the capillary induced pump mechanism. These bubbles are not explicitly modelled but simulated in an Eulerian frame as virtual bubbles tracked by a CO_2 concentration. As depicted in Fig.4, the domain is subdivided into control volumes in which the CO_2 concentration is monitored. If a sufficient amount of CO_2 has accumulated inside a control volume, a bubble is generated using mass source terms added to Eq.(3).
The initial bubble growth is a critical point within this modelling approach. If the bubble grows too quickly, very high velocities are generated because of the liquids displaced by the growing bubbles. On the other hand, if the bubble grows too slowly, during the intermediate state of growth, bubbles are too small for the CSF model and the simulation becomes instable. The time scale for initial bubble growth has been adjusted iteratively. For the present work, in each control volume 2x4x4 cells are used as source cells. The study has revealed that if bubbles grow with a dynamic filling the 8^3 cells in less than 10 time steps, the strong velocities of rapidly growing bubbles cause divergence. On the other hand, if it takes the bubbles more than 80 timesteps, the strong curvatures of bubbles filling the 2x4x4 cells cause divergence as well, now because of the high capillary pressure fluctuations. We assume that for 10 up to 80 time steps used for initial bubble growth, the dynamic forces dominate over the surface forces. At the same time, the dynamic forces are sufficiently small to allow for stability. As a compromise, a time interval of 40 time steps has been used to generate the bubbles filling 8^3 cells.

The described dynamics of initial bubble growth has nothing to do with the physics of bubble nucleation. It has exclusively been developed to introduce the bubbles into the system without causing divergence of the momentum equation (Eq.(2)). The displacement of liquid by these artificially growing bubbles certainly causes some errors within the simulation. However, as discussed later, this error is assumed to be comparably small when analysing the integral value of liquid, pumped by the movement of gas bubbles.
Once a control volume contains a gas bubble, all generated CO_2 calculated by Eq.(5) is added directly to the bubble through source terms in Eq.(3), now evenly distributed across the liquid gas interfaces occurring in each control volume. This model allows for a comparably coarse mesh where exclusively those bubbles that significantly influence the fluid dynamics are fully modelled.

4   RESULTS

The commercial CFD-code CFD-Ace+ form ESI-Group [12] is used to solve the Navier-Stokes equation on a finite volume computational grid. Additional models accounting bubble generation, bubble venting and contact angle hysteresis have been implemented as user defined functions. The presented model allows for stable simulations accounting for the interaction of bubble growth modelled by source terms, capillary transport modelled with the VoF method and a model for contact angle hysteresis [11], and gas venting approximated by sink terms [11]. The performed simulations cover a time period of one second of the operating pumping mechanism. The computational domain contains 88,264 cells in which the equations where solved by time steps of $\Delta t = 10^{-5}$s to $\Delta t = 10^{-6}$ seconds. On a single processor, the presented calculations required about three weeks. A high current density of $i = 1000$ mA cm^{-2} was applied for the simulation to make sure that a complete pumping cycle can be simulated. As in the experiments, material properties at room temperature and ambient pressure for carbon dioxide ($\rho_{CO2} = 1.78$ kg m^{-3}; $\eta_{CO2} = 1.58$ 10^{-5} kg m^{-1} s^{-1}) and for a two molar water methanol solution [13] were applied for the simulations ($\rho = 980$ kg m^{-3}; $\eta = 0.96$ 10^{-3} kg m^{-1} s^{-1}; $\sigma = 0.061$ N m^{-1}). A description of one pumping cycle and the influence of contact angle hysteresis on the capillary induced flow rates are discussed in the following.

4.1 Bubble configurations

In a first step, bubble configurations calculated with the presented model are qualitatively compared to bubble configurations captured with a camera during DMFC operation. Until now, because of different applied electrical currents within the simulations and the experimental study, a quantitative comparison is not possible. The reason for the different electrical currents is that on the one hand, the experimentally investigated DMFC does not allow for such high currents as applied to the simulations, on the other hand, the high computational effort of the simulations requires such high currents because otherwise a full pumping cycle can not be studied.

For the experiments, the channels have been made hydrophilic by dip-coating with DMAAm-MaBP [14] and the GDL was hydrophilized by plasma activation. After being freshly coated, the channel walls and the GDL exhibit very hydrophilic surfaces. Due to the almost complete wetting, the three phase contact lines are very small and contact angle hysteresis plays a minor role. As depicted in Fig.7, the simulation without accounting for contact angle hysteresis shows good qualitative agreement with the photographs. Towards the channel end, the moving bubbles increasingly block the channels. At the outlet, an average bubble length of $l = 1.5\pm0.6$mm was observed. The simulations predict an average bubble length of $l = 1.62\pm0.2$mm. The close agreement is coincidental because of the different specific electrical currents applied for the simulations and the experiments. The experimental configuration depicted in Fig.8 is the same as in Fig.7 but the picture is taken after 3 weeks of DMFC operation and testing. During this period of time, the surface coatings have degraded. Now, the simulations are performed with an assumed contact angle hysteresis of $\theta_{hys} = 40°$. The experimentally measured bubble length were about $l = 4.0\pm1$ mm and the simulations predicted $l = 3.6\pm0.1$ mm at the channel outlet. Again, because of the different flow rates, the absolute value assumed for the contact angle hysteresis is not comparable to the experimental set-up. However, qualitatively, the increase of bubble sizes with increasing contact angle hystersis because of surface coating degradation is predicted correctly by the simulations.

4.2 Pump efficiency

In Fig.9, the average liquid flow rates at the inlet of the narrow channel end are plotted against time for the configuration depicted in Fig.4. A detailed description of the bubble driven pump cycle is shown in Tab.1. The pump efficiency, defined as the ratio between the volumetric liquid flow rate to the volumetric gas flow rate is $p_{eff} = 57\%$ for the period of time considered. The negative peaks are an artefact caused by the bubble nucleation model in which the modelling of the initial bubble growth leads to rapidly growing bubbles that isotropically displace liquid out of the channel. This results in an overestimated outflow at the narrow channel end. However, the high negative flow rates occur over very short periods of time, therefore, the influence of the bubble nucleation model on the overall liquid flow rate induced by the moving bubbles is comparably small. When the bubble nucleation peaks are excluded from the calculations, the average liquid flow rate increases from $\Phi_{liquid} = 251$ µl min^{-1} to $\Phi_{liquid} = 262$ µl min^{-1} when pinning is not modelled. When pinning is considered, the flow rates increase from $\Phi_{liquid} = 95$ µl min^{-1} to $\Phi_{liquid} = 101$ µl min^{-1}. In both cases, the negative flow rate peaks caused by the bubble nucleation model reduce the pump efficiency by 2%.
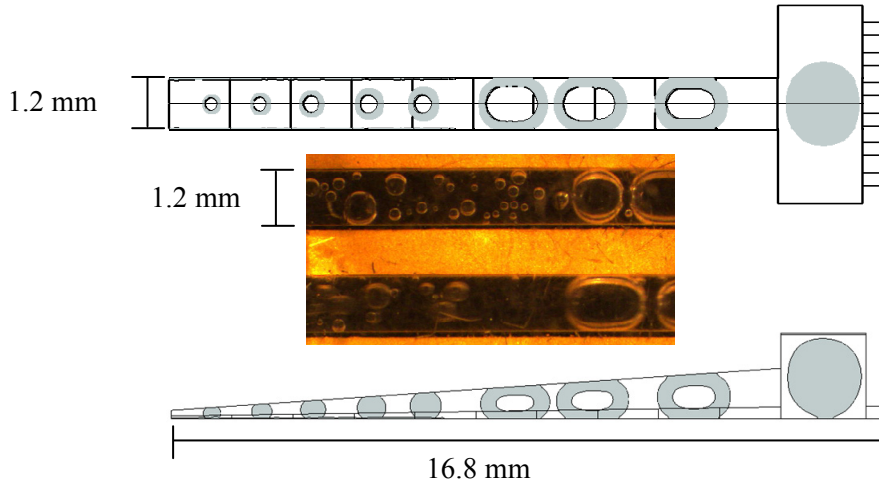
Figure 7: Bubble configuration in a tapered channel flow field.
Simulation: Moving bubbles without accounting for contact angle hysteresis. $\theta_s = 10°$; $i = 1000$ mA cm^{-2}.
Experiments: Passive operating DMFC: $i = 115$ mA cm^{-2}. Channel walls have been made hydrophilic by dip-coating with DMAAm-MaBP and the GDL has been made hydrophilic by plasma activation.
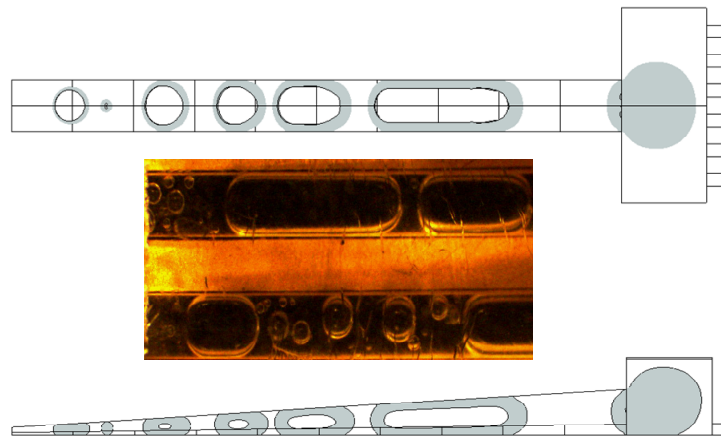

Figure 8: Bubble configuration in a tapered channel flow field of a DMFC tested for three weeks.
Simulation: Moving bubbles accounting for contact angle hysteresis. $\theta_s = 10°$, $\theta_{hys} = 40°$, $i = 1000$ mA cm^{-2}.
Experiments: Passive operating DMFC: $i = 115$ mA cm^{-2}. Channel walls have been made hydrophilic by dip-coating with DMAAm-MaBP. The GDL has been made hydrophilic by plasma activation. The DMFC has been tested and operated for three weeks. The surface coating has degraded, thus contact angle hysteresis is present leading to the larger bubbles.
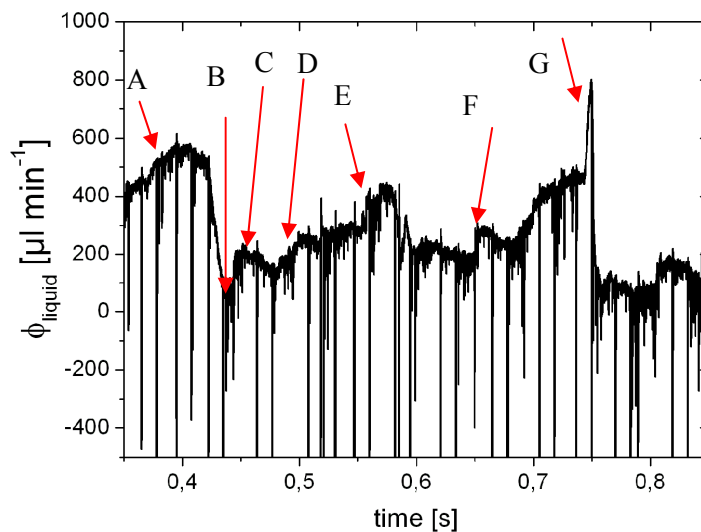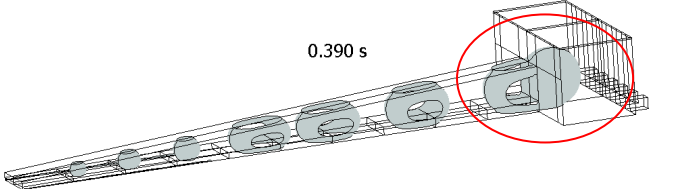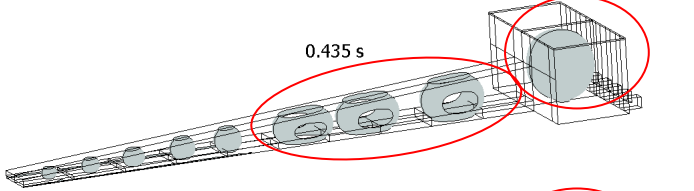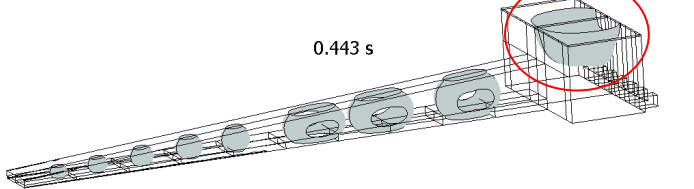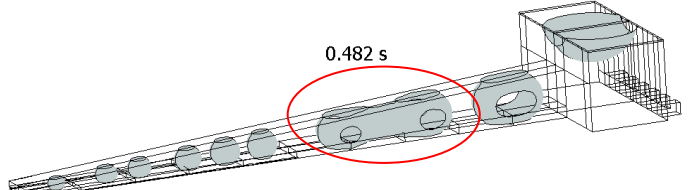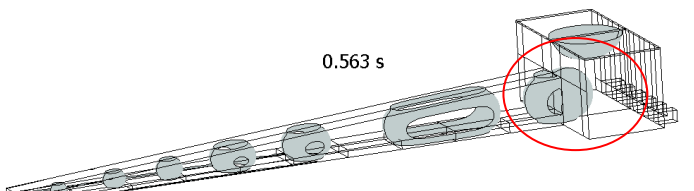

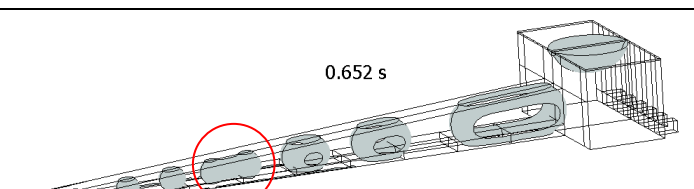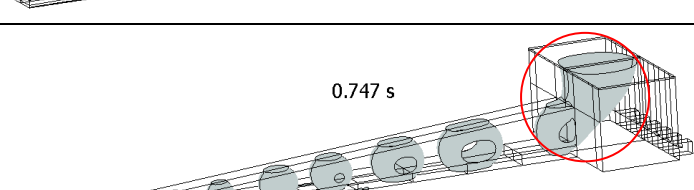**Figure 9:** Liquid flow rate induced by moving bubbles plotted against time at a current density of $i = 1000$ mA cm^{-2}. The average pump efficiency of the period of time plotted was $p_{eff} = 57\%$. Contact angle hysteresis is not considered.

A	0.390 s	A bubble moves from the tapered channel into the gas collection channel. The interface curvature changes abruptly and surface energy is converted into kinetic energy causing the high flow rates in section A.
B	0.435 s	The large bubble now forms a sphere in the gas collection channel not contributing to the pumping mechanism. The comparably low flow rate in section B is induced by the movement of the three small blocking bubbles in the tapered channel.
C	0.443 s	Now the large bubble is attached to the porous membrane and venting takes place. Liquid replaces the vented gas, therefore the liquid flow rate increases in section C.
D	0.482 s	In section D, the merge of two bubbles temporally increases the flow rates. Because of the larger curvatures of the bubble in the narrower part, during the merge the rear bubble "jumps forward" and thereby drags liquid into the channel.
E	0.563 s	Again a bubble moves from the tapered channel into the gas collection channel. The flow rate increases. Because of the smaller volume of this bubble the peak is smaller than in section A.
F	0.652 s	A bubble merge occurs and the flow rate is increased again. The bubbles are smaller than in section D. Therefore, the temporary increase of flow rate is smaller as well.
G	0.747 s	Here, the gas bubble reaching the hydrophobic membrane reaches back into the tapered channel. The shrinking bubble directly sucks liquid into the channel leading to the peak in liquid flow rates.

Table 1: Several phenomena influencing the pumping performance. Contact angle hysteresis not considered.

Adding the model for contact line pinning with a contact angle hysteresis of $\theta_{hys}= 40°$ causes a decrease of the pump efficiency by 35% which can be explained as follows: Due to contact line pinning, the gas bubbles are less mobile which increases the overall gas load in the channels. The higher gas load results in fewer and smaller liquid segments enclosed by the moving gas bubbles. Therefore, as illustrated by the graph in Fig.10, less liquid is transported through the considered tapered channel and the overall pump efficiency reduces from p_{eff} = 57% to p_{eff} = 22% when the contact angle hysteresis increases from $\theta_{hys}= 0°$ to $\theta_{hys}= 40°$. Details of the pump cycle with contact line pinning modelled are discussed in Tab.2.

In our previous work [5], it was experimentally identified that in a different channel geometry, contact line pinning can also increases the flow rates because of the resulting blocking pumping mode as further detailed in [5]. These experiments were performed in channels with a much larger cross section. For the

configuration investigated here however, the blocking pumping mode already occurs in the middle of the channel even if no contact angle hysteresis is present (see Fig.7). Consequently, contact angle hysteresis only slightly changes the pumping mode, in particular close to the inlet. Thus, a variation of liquid flow rates because of a change of pumping modes could not be observed in this study.

For the operating DMFC, the minimum pump efficiency required to sustain DMFC operation yields:

$$p_{eff,min} = \frac{\rho_{CO_2}}{M_{CO_2} C_f} \qquad (6)$$

where M_{CO2} is the molecular weight of CO_2, C_f is the molar concentration of the water-methanol solution and ρ_{CO2} is the density of carbon dioxide. In the present work, a methanol concentration of the water methanol solution of 2 mol L^{-1} has been investigated. The minimum required pump efficiency is therefore $p_{eff} = 2.0\%$. Thus, the simulation study shows that the proposed passive supply mechanism pumps enough methanol even if contact angle hysteris on the channel surfaces increases due to surface coating degradation.
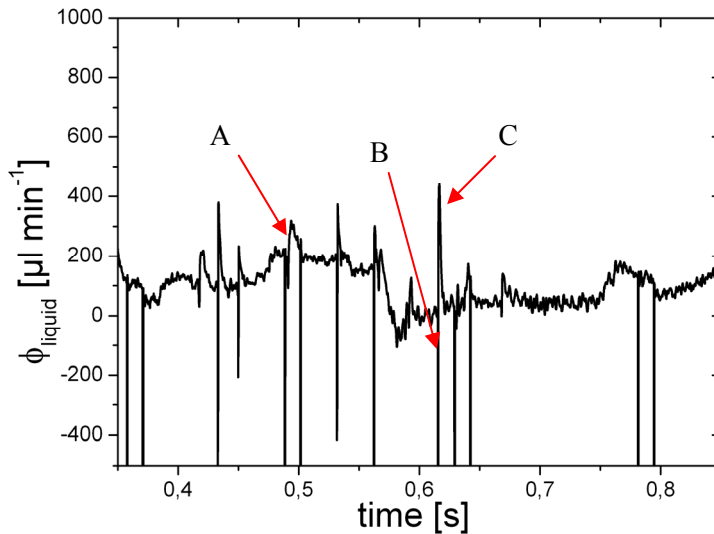

Figure 10: Liquid flow rate induced by moving bubbles plotted against time. $i = 1000$ mA cm^{-2}. The average pump efficiency of the period of time plotted was $p_{eff} = 22$ %. The simulation includes contact angle hysteresis.

A		As in the simulations without hysteresis, the bubble moving from the tapered channel into the gas collection channel increases the induced flow rate. The bubbles are much larger and due to contact angle hysteresis less mobile. Therefore, the peak flow rate is with 300 µl min^{-1} about half the size as in the simulation without hystersis.
B		A new bubble grows, liquid is displaced in all directions and the flow rate is negative. The direction of bubble movement has turned around. The previously advancing meniscus is now a receding one and vice versa.
C		The bubble growth is finished and the direction has changed again. The back and forth flipping of the interface causes the positive peak in flow rates.
Table 2: Several phenomena influencing the pumping performance with contact angle hysteresis modelled.		

4. CONCLUSION

CFD simulations of a passive supply mechanism on the anode of a DMFC are presented. Passive fuel supply is achieved by utilizing the capillary movement of CO_2 bubbles, generated as a reaction product during DMFC operation. The moving bubbles pump methanol for the supply of the DMFC. The model includes bubble generation, capillary induced movement of bubbles with contact angle hysteresis and venting through a porous membrane. The focus of the present study is to investigate the different phenomena contributing to the liquid flow rates induced by the moving bubbles. Bubble merge was identified to temporarily increase the liquid flow rates and therefore supports the pumping mechanism. Bubble venting supports the pumping mechanism as well. High flow rates occur when a moving bubble reaches the end of the tapered channel and transfers into the gas collection channel. If contact angle hystersis is present, the bubbles are larger and less mobile. This leads to lower pump rates. In our case, the pump efficiency decreases from p_{eff} = 57% to p_{eff} = 22% when a contact angle hysteresis increases from θ_{hys} = 0° to θ_{hys} = 40°. Since the minimum required value for DMFC supply is p_{eff} = 2.0 %, at least 11 times more methanol than critically needed is pumped by the proposed mechanism.

In future works, an improved model for bubble generation will be addressed that already accounts for the displacement of liquid when bubbles are small and simulated as a CO_2 concentration within the Eulerian frame. Further more, a direct comparison of experimental data and simulations are planned. Preconditions for such comparisons are equal electrical currents. This can either be achieved by further reducing the computational effort of the simulations or by setting up experiments that allow for such high electrical currents as applied in the presented simulation study.

ACKNOWLEDGEMENTS

BIBLIOGRAPHY

[1] R. Chen, T. S. Zhao, and J. G. Liu, "Effect of cell orientation on the performance of passive direct methanol fuel cells," *J. Power Sources*, vol. 157, no. 1, pp. 351-357, June2006.

[2] T. Shimizu, T. Momma, M. Mohamedi, T. Osaka, and S. Sarangapani, "Design and fabrication of pumpless small direct methanol fuel cells for portable applications," *J. Power Sources*, vol. 137, no. 2, pp. 277-283, Oct.2004.

[3] Y. H. Chan, T. S. Zhao, R. Chen, and C. Xu, "A small mono-polar direct methanol fuel cell stack with passive operation," *J. Power Sources*, vol. 176, pp. 183-190, Dec.2007.

[4] T. K. Yeh and Chen C.H., "Modeling and optimizing the performance of a passive direct methanol fuel cell," *J. Power Sources*, vol. 175, pp. 353-362, 2008.

[5] N. Paust, C. Litterst, T. Metz, R. Zengerle, and P. Koltay, "Fully Passive Degassing and Fuel Supply in Direct Methanol Fuel Cells," in *Proceedings of the 21st IEEE International Conference on Micro Electro Mechanical Systems, MEMS* Tucson, USA: 2008, pp. 34-37.

[6] J. H. Ferziger and M. Peric, *Computational Methods for Fluid Dynamics*, 3rd rev. ed Springer, 2002.

[7] C. W. Hirt and B. D. Nichols, "Volume of Fluid (Vof) Method for the Dynamics of Free Boundaries," *Journal of Computational Physics*, vol. 39, no. 1, pp. 201-225, 1981.

[8] W. J. Rider, D. B. Kothe, S. J. Mosso, J. H. Cerutti, and J. I. Hochstein, "Accurate Solution Algorithms for Incompressible Multiphase Flows," Presented at the 33rd AIAA Aerospace Science Meeting and Exhibit,AIAA-95-0699, Oct.1994.

[9] J. U. Brackbill, D. B. Kothe, and C. Zemach, "A Continuum Method for Modeling Surface-Tension," *Journal of Computational Physics*, vol. 100, no. 2, pp. 335-354, June1992.

[10] L. C. Gao and T. J. McCarthy, "Contact angle hysteresis explained," *Langmuir*, vol. 22, no. 14, pp. 6234-6237, July2006.

[11] N. Paust et. al., "A Computational Fluid Dynamics (CFD) model for capillary two phase flow with relevance to fuel transport in passive Direct Methanol Fuel Cells (DMFCs), submitted to *Computers and Fluids*.

[12] www.esi-group.com/products/Fluid-Dynamics/cfd-ace

[13] R. L. Lide, *Handbook of Chemistry and Physics*, 82nd ed. Boca Raton, USA: CRC Press, 2001.

[14] R. Toomey, D. Freidank, and J. Rühe, "Swelling Behavior of Thin, Surface-Attached Polymer Networks," *Macromolecules*, vol. 37, pp. 882-887, 2004.